Millimeter-Wave System for High-Speed Train Communications Between Train and Trackside: System Design and Channel Measurements

Guangrong Yue, Daizhong Yu, Long Cheng, Qifu Lv, Zhigang Luo, Qing Li, Junxin Luo, and Xu He

***Abstract*—This paper introduces the design of a 41 GHz mmWave system dedicated for high-speed train communications between train and trackside. A novel frame structure is provided for the acquirement of channel state information as well as for the transmission of user data. Based on the proposed design principles, a system prototype has been established and employed in extensive measurement campaigns. The channel measurement results obtained from a recent measurement campaign under high-speed mobile conditions where the relative velocity between the transmitter and the receiver reaches 170 km/h are presented in this paper. Channel characteristics, including the power delay profile, RMS delay spread, fade depth, small-scale fading statistics, Ricean *K* factor, autocovariance function, coherence time, level crossing rate, and average fading duration are analyzed in detail. Moreover, the bit-error-rate performance for the proposed system under the channel whose characteristics are obtained from the measurements is simulated. Based on the simulation results, the key parameters for the proposed frame structure are determined to improve the system's robustness in fast varying channels and in the mean time achieve high spectrum efficiency. Besides, the throughput of the system prototype recorded during the transmission of three high-definition video streams is presented. Finally, the outage probability as a function of transmission distance and path loss exponent is estimated based on the channel measurement results.**

***Index Terms*—mmWave system, HST communication, measurement campaign.**

I. Introduction

As a GREEN and efficient transportation model, high speed rail (HSR) has been expanding rapidly in Europe and Asia. Along with the expansion of HSR, the population of passengers using various portable smart devices (e.g., laptops, smart phones) crowded on the train has also been growing rapidly. To enhance the safety and the experience of passengers, high speed train (HST) communications should not only handle the critical signalling applications, but also provide various broadband services, such as high definition (HD) video surveillance, stable on-board broadband Internet access, real-time train dispatching video, journey information, and Internet of Things (IoT) for railways [1], [2].

As the global system for mobile for rail (GSM-R) can only support a maximum data rate of less than 200 kbps [3], it cannot meet the requirement of high-data-rate transmissions. To enhance data transmission rate and provide broadband wireless access for HST, a large number of technologies have been presented, such as long-term evolution advanced (LTE-A) networks [4], WiMax on rails [5], IEEE 802.11 [6], and LTE for railway (LTE-R) [7]. However, these current technologies support data rates range from Mbps to 100 Mbps, which is insufficient to meet the requirements of future rail transport where infrastructure, trains, travelers, and goods are expected to be interconnected [1], [8].

One of the potential solutions to realize high-data-rate transmission is employing millimeter wave (mmWave) communications in HST services [1], [9], [10]. Owning to the vast spectrum resources at mmWave bands (e.g., 28 GHz, 40 GHz, and 60 GHz, etc. [11]–[14]), mmWave is an attractive technology to provide high-data-rate transmission with throughput of Gbps level, and thus becoming a potential candidate for the fifth generation (5G) wireless systems [15], [16]. Hence, it has been proposed that mmWave technologies should be applied in railway communication scenarios to meet the high-data-rate demand for future railway networks [17].

The feasibility and potentiality of mmWave communications as a promising candidate for HST communications has also been validated by recent studies. For example, in the work of Junhyeong Kim *et al.* [2], a comprehensive design of a mmWave-based mobile hotspot network (MHN) system has been provided for two different prototypes, named MHN conventional (MHN-C) and MHN enhanced (MHN-E), for which field trials and simulations have been carried out to show that a peak down link throughput of 7 Gbps can be achieved with the single-frequency multi-flow (SFMF) transmission scheme when the train's speed is up to 500 km/h.

Besides the work of [2], there are numerous studies focusing on the channel characteristics for HST scenarios at mmWave bands by methods of measurements and simulations [18]–[22].

Manuscript received March 16, 2018; revised June 15, 2018, October 9, 2018, and January 20, 2019; accepted May 8, 2019. Date of publication May 31, 2019; date of current version December 17, 2019. This work was supported in part by the National Natural Science Foundation of China under Grant 61831004, in part by the Defense Industrial Technology Development Program under Grant JCKY2016204A603, and in part by the National Defense Science and Technology Innovation Special Zone Project of China. The review of this paper was coordinated by the Guest Editors of the Special Section on Smart Rail Mobility. *(Corresponding author: Daizhong Yu.)*

G. Yue, D. Yu, L. Cheng, and X. He are with the National Key Laboratory of Science and Technology on Communications, University of Electronic Science and Technology of China, 611731 Sichuan, China (e-mail: yuegr@uestc.edu.cn; 15908107465@163.com; chenglong_office@163.com; hexu@uestc.edu.cn).

Q. Lv, Z. Luo, Q. Li, and J. Luo are with Glory Wireless Corporation Limited, 610094 Sichuan, China (e-mail: 1203437767@qq.com; lzg0179@163.com; 365182130@qq.com; luojunxin@163.com).

Digital Object Identifier 10.1109/TVT.2019.2919625

For example, in the work of Danping He *et al.* [18], channel measurements and ray tracing simulations have been conducted in the 5G mmWave bands (the 25 GHz band and 30 GHz band) to study the propagation characteristics, including path loss, root-mean-square (RMS) delay spread, Ricean *K* factor, etc., for HSR urban, rural and tunnel environments.

Moreover, to deal with the problems brought by the high mobility of the train, including the fast fading channel, large Doppler spreads, and frequent handover, a great number of novel technologies for mmWave communications have been developed, such as distributed antenna system (DAS) [23], radio on fiber (RoF) [24], hybrid beamforming [25], beam switching [26], and antenna hopping [27], etc., to achieve a good compromise between performance and complexity.

However, given all these studies mentioned above, the implementation of mmWave for HST still faces many challenges. The first challenge of all is a lack of research on channel measurements and modelling [2], [18]. On the one hand, most channel measurement campaigns for HST scenarios have been mainly conducted at frequencies below 6 GHz [28]–[32]. On the other hand, most mmWave band measurements are conducted for urban outdoor and indoor environment where the relative speed between the transmitter and the receiver is assumed to be lower than 10 km/h [33]–[35]. Due to the difficulty in conducting channel measurement at high moving speeds and the lack of readily available mmWave systems dedicated for HST communications, the channel characteristics in various HST scenarios have been investigated mainly through ray tracing simulations [1], [2], [18]–[22].

In this paper, we introduce the design of a mmWave system operating at the 41 GHz band for HST communications. A novel and simple frame structure is proposed for the acquirement of channel state information (CSI) and the transmission of user data. Based on the proposed design principles, a system prototype has been established and employed in extensive channel measurements. To explore the channel characteristics when the transmitter (TX) and receiver (RX) are moving at high speeds, a measurement campaign has been carried out recently where the relative speed between TX and RX reaches 170 km/h. The measurement and analysis results, including the power delay profile (PDP), RMS delay spread, fade depth, small scale fading statistics, Ricean *K* factor, autocovariance function, coherence time, level crossing rate and average fading duration, are also presented in this paper. Moreover, the measured channel characteristics are employed in the simulation which exhibits the bit-error-rate (BER) performance of the proposed system and determines some key parameters in the frame design to improve the system's robustness in fast varying channels and in the meantime to maximize spectrum efficiency. The system throughput recorded during the transmission of three high-definition video streams with the system prototype is also presented in this paper. At last, the outage probability of the proposed scheme is estimated based on the channel measurement results.

The rest of this paper is organized as follows. In Section II, an overview on the application of mmWave technologies on HST communications is provided. In Section III, the system design principles combined with a hardware prototype for the proposed system are presented in detail. Section IV gives the measurement results obtained from a recent measurement campaign. The BER performance, system throughput and outage analysis is provided in Section V. At last, a conclusion is drawn by summarizing the work and giving the possible directions of our future research.

In this paper, $N\left(\mu, \sigma^2\right)$ denotes the normal distribution with mean μ and variance σ^2, and $N_{log}\left(\mu, \sigma^2\right)$ denotes the lognormal distribution where μ and σ are the mean and standard deviation for the corresponding normal distribution, respectively.

II. Overview on mmWave HST Communications

In this section, an overview on mmWave HST communications is provided. We focus on four important aspects of mmWave HST communications: the channel characteristics, the network structure, the beamforming strategies, and the handover schemes.

A. Channel Characteristics

The propagation of mmWave frequencies is characterized by the large attenuation as a result of small wavelength, atmosphere attenuation, rain attenuation, and penetration loss.

At first, the wavelength of mmWave signals ranges from 1 mm to 10 mm, which is much smaller than that of sub-6 GHz systems. As a result, mmWave frequencies will undergo greater free space attenuation in the first meter of propagation due to the Friis' free space equation [33], [36]. However, measurements by T. S. Rappaport *et al.* and Smulders *et al.* [33], [37] have shown that the path loss exponents (PLEs) (i.e., power decays as the square of the distance) at numerous mmWave bands exhibit no much difference from the PLEs at ultra high frequency (UHF) bands.

Apart from the free space attenuation, atmosphere and rain will also have frequency-dependent attenuation effects on mmWave propagation. Atmosphere attenuation across most of the mmWave spectrum induces merely a few dB of additional loss per kilometer distance [36]. However, at certain mmWave bands, such as the 60 GHz band, the molecular resonances can contribute an additional path loss of up to 15 dB per km distance [38], [39]. For most mmWave bands, rain attenuation will only lead to a few dB of additional path loss within the distance range of 1 km. More explicitly, the additional rain attenuation is within 20 dB/km at frequencies less than 100 GHz when the rain rate is less than 50 mm/h [40].

The impact of the atmosphere and the rain can be mollified through the use of high-gain, narrow-beam antennas [33]. High gain and narrow-beam antennas can not only realize long-distance transmission, but also reduce the delay spread of the wireless channel. The measurement work of M. Kyro *et al.* has revealed that when highly directive antennas are used for long range communications, the delay spreads are no more than 10 ns relative to the line-of-sight (LoS) component when transmitting over 500 MHz of bandwidth [41]. As for HST communications, the distance between adjacent base stations (BSs) should be as large as possible to reduce the handover frequency, so the communication distance between the BS and the train is often as

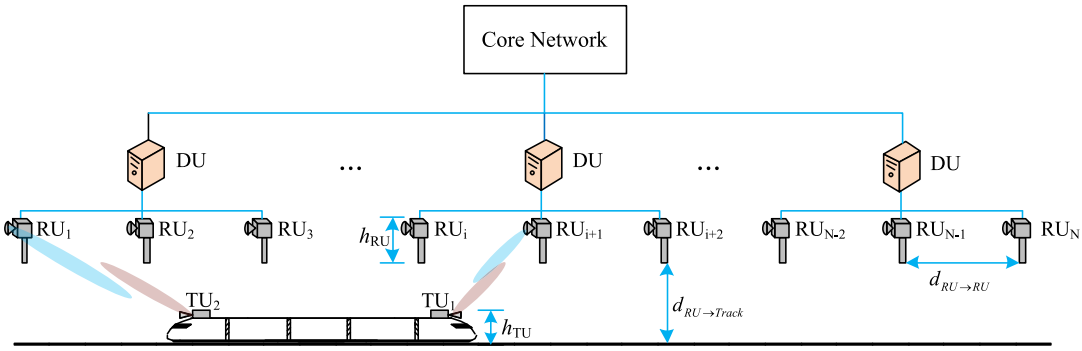

Fig. 1. Typical network architecture for mmWave HST communications.

long as hundreds of meters. Thus, high-gain antennas or antenna arrays with beamforming techniques are preferable for HST mmWave communications.

Another feature of mmWave propagation is its susceptibility to blockage. It has been shown by measurements that human blockage can create more than 40 dB of fading for mmWave transmission [39], [42]. Penetration through water, glass, mental, and foliage will also lead to considerable loss to the propagation of mmWave signal [43], [44]. Hence, it is more preferable that mmWave be used for high capacity mobile backhaul wireless (MBW) links in HST communications rather than the direct links between passengers inside the carriage and the BSs outside [2].

In HST communications, the typical railway environments can be classified into a number of special scenarios such as viaducts, cuttings, tunnels, stations, urban environments and rural environments [45]. To cope with the fast speed of the train, HSR lines are constructed with gentler curves, wider cuttings, and wider tunnels compared with their conventional counterparts [46]. These differences might result in significant changes in channel characteristics. Besides, wireless channel characteristics can differ significantly in different HST scenarios [18].

Due to the fast moving speed of HST (e.g., up to 500 km/h), the wireless channels for high speed railway are significantly different from conventional wireless channels for cellular networks where the moving speed of user equipments (UEs) is usually less than 10 km/h. In general, the wireless channels in conventional cellular networks are often assumed to be wide-sense stationary uncorrelated scattering (WSSUS) [47]. However, this assumption might not hold for HST communication, where the wireless channel is characterized by its rapid time-varying and nonstationary features [47]. Besides, if trackside BSs with directional antennas are deployed, LoS can be maintained in most of the HST scenarios. As a result, there might be large spatial correlation between different multipath elements, resulting in correlated scattering [47].

B. Network Structure

Fig. 1 gives the typical dual-hop directional network architecture for mmWave HST communications composed of user access links inside the train and mobile wireless backhaul links outside. Multiple radio units (RUs) are deployed along the railway track and equipped with radio frequency (RF) transceivers and beamforming (BF) antennas for generating and receiving directional mmWave beams via analog or digital techniques. The digital units (DUs) interconnected with one or multiple RUs can offer physical layer processing, traffic offloading, latency reduction, inter-RU management, and communicate with the public Internet via the core network [2], [9]. The terminal units (TUs) installed inside or on top of the train serves as mobile relays that communicate with trackside RUs via high capacity mmWave links. Usually, two TUs are considered in the system, with one TU placed at the front side and another TU at the rear side of the train. Those two TUs can either communicate with different DUs to achieve additional multiplexing gain [2] or with the same DU to maintain the link stability and achieve additional diversity gain [48]. Onboard access point (APs) of Wi-Fi or small cell connected to the TU can be then set up in the train to provide on board users with mobile Internet accesses. This network architecture for mmWave HST communications is adopted by the mmWave-based mobile hotspot network (MHN) system [2] and the 3GPP 5G new radio (NR) HST system [9].

The cell size and the inter-RU distance depend, to a great extent, on the operating frequencies. For instance, in 3GPP NR HST systems [49]–[51], both the frequencies of 4 GHz and 30 GHz are employed. Consequently, the cell size is 1732 m, which is the cell size for both of the 4 GHz and 30 GHz scenarios, and each cell contains three evenly placed RUs to maintain the same attenuation level for the 30 GHz system as in the 4 GHz system. The inter-RU distance $d_{RU\rightarrow RU}$ is chosen as 580 m and 572 m to maintain approximately equal inter-RU distance. Generally, the heights of the antennas mounted on TUs on the train and on RUs along the trackside (h_{TU} and h_{RU} in Fig. 1) are about 3 m and 5–7 m, respectively. The distance between RUs and the railway track ($d_{RU\rightarrow Track}$) is usually 5 m [9].

The network will have various specific features based on the techniques employed. For example, in radio on fiber (RoF) mmWave systems [52], [53], up-link and down-link wireless services are digitalized to baseband (BB) signals and processed in the DU which is shared by multiple RUs via the wavelength-division multiplexing (WDM) RoF links. As all expensive and intelligent signal processing units are located at DUs, the RUs can be very simple. This can help significantly simplify the system and reduce the cost, power consumption and latency.

In MHN-enhanced (MHN-E) systems, it is recommended in [54] that single frequency network SFN with beamforming techniques be considered in HST system to mollify the problem of frequent handover. Further, it is suggested that a RU be shared with adjacent DUs so that the inter-DU handover is performed after the TU is connected to the shared RU, which can not only maintain the communication link but also provide sufficient time for the handover.

C. Beamforming Schemes

Thanks to the small wavelengths in the mmWave regime, large antenna array architectures can be embedded into communication devices with a compact form factor, making beamforming an attractive proposition. Essentially, beamforming (BF) is a spatial filtering operation typically using an array of radiators to capture or radiate energy in a specific direction over its aperture [55]. In mmWave systems, antenna beamforming assumes a pivotal role in not only maintaining a robust communication link and increasing the link capacity , but also improving the channel conditions in terms of increasing signal-to-noise ratio (SNR) gain, enhancing Ricean factor gain, and reducing RMS delay spread with directional communication [56]. *Digital beamforming* refers to the beamforming technique where the beamforming process is done at the digital baseband, whereas *analog beamforming* is a beamforming approach that relies entirely on the RF domain process. Compared with analog beamforming, digital beamforming has the advantage of greater flexibility and larger freedom in implementing efficient beamforming algorithms [55], but suffers from much higher complexity, power consumption and cost, especially in large-scale antenna systems (LSAS) [57]. Thus, an alternative choice named hybrid beamforming utilizing a hybrid analog and digital structure has emerged as a key enabler to flexible beamforming with low cost and multi-stream, multi-user transmissions [57], [58]. A comprehensive survey on beamforming for mmWave communications can be found in [55].

For HST communications, two BF schemes can be employed by eighther RU or TU: the *fixed BF* where the antenna weight parameters are fixed during BF communications, and the *adaptive BF* where the antenna weight parameters can be continuously updated based on the received signals [59]. As a result, during the communication process, the beam of the fixed BF is set to the pre-determined direction and cannot be changed whereas adaptive BF can adjust its antenna beam to follow the angle of the target signal. In the simulation analysis in previous studies [1], [54], [60], it is shown that applying adaptive BF to both RU and TU can improve the channel capacity and enhance the signal-to-interference-plus-noise-ratio (SINR) when TU is close to RU. However, it can also be observed that the performance gain by applying adaptive BF decreases and gradually becomes negligible as the TU moves far away from the DU. As the linear structure of HST cells makes the beam easier to cover the railway track even though the beam width is small, it is sufficient to apply the fixed BF to both TU and RU most of the time from the implementation feasibility and performance perspectives [54]. Besides, sophisticated adaptive BF methods have not been extensively used so far in mmWave communications due to increased signal processing overheads and latency, and the performance of practical adaptive BF highly depends on the calibration error, which is often not taken into account in simulations [60]. Hence, it is proposed in [60] that the scheme where adaptive BF is only used at the receiver (RX) instead of at both the transmitter (TX) and the receiver (RX) be applied to achieve a good compromise between system complexity and performance.

D. Handover Schemes

Handover is a big challenge for mmWave HST communications. At first, the transmission of mmWave signal will undergo severe propagation loss for several reasons mentioned in Section II-A. Hence, the coverage of the signal is limited, resulting in small cells. Combined with the fast speed of the train that reaches up to 500 km/h, the handover is more frequent and serious in HST communications than that in the traditional cellular networks [48]. Secondly, since mmWaves are highly susceptible to blockage, obstacles such as passing trains, arched grids, wind barriers, and the acoustic barriers along the railway tracks can cause the mmWave channel to rapidly appear or disappear due to obstruction. Moreover, to enhance the channel capacity and system reliability, a novel communication system based on control/user (C/U) plane split heterogeneous networks is a current hot spot and is highly possible to be employed in high-speed railways [48], [61]. In the C/U plane split network, the control (C) plane information and the user (U) plane information are transmitted separately at different frequency bands: the C plane information at the lower frequency band (e.g., the 930-934 MHz and 885-889 MHz that are previously allocated to GSM-R) and the U plane information at the mmWave bands so that the C plane will not interfere with the U plane. However, this C/U split architecture poses greater challenges on handover, because the handover needs to be operated in both C plane and U plane, which will lead to higher handover frequency and larger outage probability [61].

To reduce handover latency and attain robust seamless handover for HST communications, a number of novel handover techniques have been presented in the literature. For example, applying the idea of macro-diversity [62], [63], J. Zhao *et al.* proposed a dual-link soft handover scheme for C/U plane split network [48], where two TU antennas are installed at the front and the rear of the train. When the train is located in a single cell, those two antennas are used to achieve larger diversity gain. As the train is travelling across the cell edge, handover is performed by the two antennas separately to realize seamless handover and reduce the handover failure possibility. In [64], Yang Lu *et al.* argued that although applying two antennas on the train can release the problem of frequent handover, the seamless handover is still difficult to be ensured when the base stations (BSs) are relatively far away from the train due to the near-far signal propagation effect. Thus, it is proposed in [64]–[66] that the distributed antenna system (DAS) architecture be applied to HSR handover schemes to reduce the BS-train distance. To further address the handover failure problem caused by frequent handover in DAS-based handover schemes for HSR,

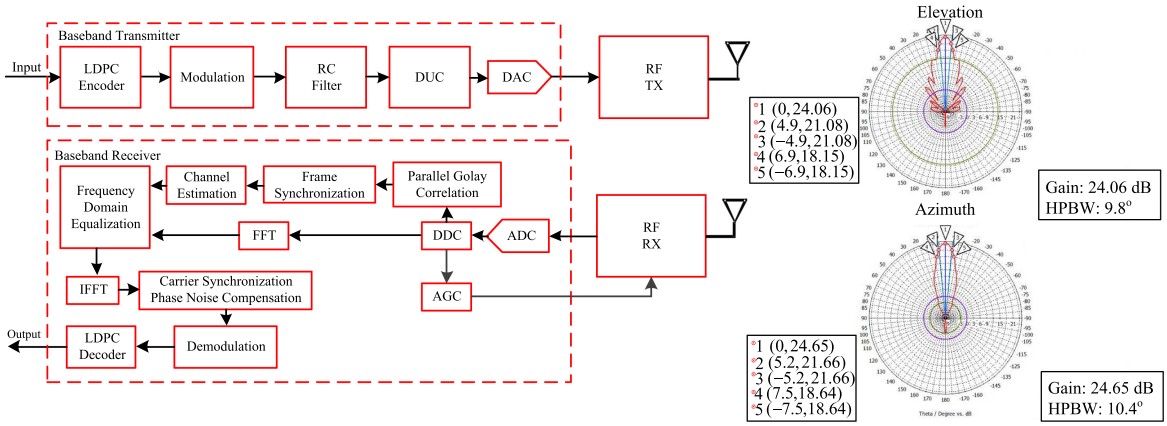

Fig. 2. Transceiver architecture and antenna patterns.

Junhyeong Kim *et al.* propose in [67] that a RU be shared by adjacent DUs (cells) such that the inter-cell handover is triggered when the TU is connected to the shared RU, thus attaining sufficient time for handover processing and minimizing handover failure probability. The research in [67] indicates that the advantages of DAS can be further exploited to improve the handover performance.

III. System Design

In this section, the design principles of the proposed system for mmWave HST communications are presented. The involved respects are: the system architecture, beamforming strategy, frame structure, frame synchronization, channel estimation, equalization and LDPC decoding. In the last subsection, we introduce the hardware prototype established based on the discussed principles. The key parameters of the hardware prototype are also given, which are of great importance for the analysis in the following sections.

A. System Architecture

Fig. 2 depicts the transceiver architecture. To guarantee the performance and lower the cost of this system, we employ a number of time-tested technologies, such as Golay sequence based frame synchronization [68]–[70], channel estimation based on Golay correlator [71], [72], frequency domain fractionally spaced equalization (FD-FSE) [73]–[76], and LDPC decoding based on stochastic computing [77]–[81]. On top of these technologies, we adopt a simple single carrier frequency domain equalization (SC-FDE) architecture.

On the transmitter side, The LDPC encoded bits are mapped to quadrature phase shift keying (QPSK) symbols, pulse shaped, and then up converted to 3 GHz intermediate frequency (IF) in the digital baseband. A digital-analog converter (DAC) then converts the 3 GHz digital signal into analog form, which is up converted to 41 GHz mmWave band in the radio frequency (RF) front-end.

On the receiver side, the reverse process is performed. In the RF front-end, the 41 GHz mmWave signal is at first down converted to the IF band, which is 1 GHz. We adopt different TX and RX IFs to avoid the co-channel interference between TX and RX. In the digital baseband, the digital down conversion (DDC) module converts the 1 GHz IF signal down to baseband digital signal, from which Golay sequences are identified and extracted for channel estimation. The parallel fast Fourier transform (FFT) module transforms the time-domain signal and channel impulse response (CIR) into frequency domain. Frequency domain equalization (FDE) instead of time domain equalization (TDE) is applied due to the concern of the wide bandwidth of the mmWave channel. The equalized symbols are then fed to the QPSK demodulation module, after which LDPC soft decoding is conducted and user data streams can then be obtained.

B. Beamforming Strategy

We employ high-gain narrow-beam antennas in the system design to cope wih the large attenuation at mmWave frequencies. Although it is mentioned in Section II-C that the most desirable beamforming strategy might be using fixed BF at TX and adaptive BF at RX, we adopt only the fixed BF strategy for both TX and RX for the following reasons:

1) adaptive BF technologies for mmWave HST communications is still in the theoretical research stage and is often based on a number of ideal assumptions such as ideal calibration. From the perspective of implementation, using fixed BF can reduce the uncertainties caused by the disagreement between ideal assumptions and practical cases.
2) sophisticated adaptive BF algorithms will tremendously increase the system complexity and system cost, whereas fixed BF appears to be more feasible from the cost efficiency perspective at the expense of acceptable performance loss [60];

Fig. 2 gives the antenna beam pattern at the 41 GHz band. Important points, including the point with the highest gain (point 1), the -3 dB points (point 2 and 3) and the -6 dB points (point 4 and 5) are marked out with "$\odot$" and denoted in the form of $(direction, gain)$. It can be seen that the antenna gain reaches above 24 dBi at 0° in both the elevation and azimuth phases, and the elevation and azimuth half power beam-width (HPBW) are 9.4° and 10.8°, respectively.

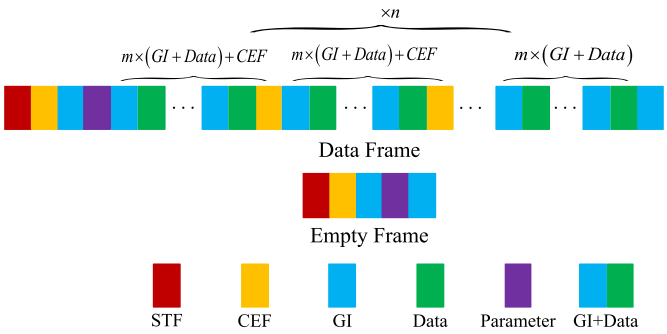

Fig. 3. Proposed frame structure for mmWave HST communications.

C. Frame Structure

Fig. 3 depicts the frame designed for mmWave HST communication. The basic elements, including the short training field (STF), the channel estimation field (CEF) and the guard interval (GI) are composed of a pair of length-128 complementary Golay sequences [68], denoted as Ga_{128} and Gb_{128} in this paper.

A STF consists of sixteen Ga_{128}'s and one $-Ga_{128}$: $STF = (rep\,(Ga_{128}, 16)\,, -Ga_{128})$, where the function $rep\,(Ga_{128}, 16)$ means repeating Ga_{128} 16 times. The periodic feature of STF have proven to be crucial for coarse frame synchronization [69] at the receiver.

A CEF is a length-512 Golay sequence

$$(Gb_{128}, Ga_{128}, -Gb_{128}, +Ga_{128})\,, \tag{1}$$

and is used for channel estimation by applying the feature of complementary Golay sequences that the sum autocorrelation of two complementary sequences will have a unique peak and zero sidelobe, denoted as

$$\begin{aligned} R_a\,(i) \; + R_b\,(i) &= 2N\delta\,(i)\,; \\ R_a\,(i) \; &= \sum_{k=0}^{N} Ga_N\,(k) Ga_N\,(i+k)\,; \\ R_b\,(i) \; &= \sum_{m=0}^{N} Gb_N\,(m) Gb_N\,(i+m)\,; \end{aligned} \tag{2}$$

where N denotes the length of each Golay sequence and $\delta\,(i)$ denotes the Dirac-delta function. (2) indicates that an impulse of energy $4N^2$ can be generated by computing the sum of the autocorrelations of sequences Ga_N and Gb_N. An efficient approach of implementing (2) is through parallel matched filtering [71], [72].

A GI is composed of the last 64 symbols of Ga_{128}. GIs protects the user data blocks against inter-symbol interference (ISI). The GI block is also of great use for phase and frequency offset compensation. The receiver performs auto-correlation between the received GI and the locally stored GI to estimate the phase rotation of each $GI + Data$ block, during the time of which the phase rotation caused by phase noise and frequency offset can be assumed as invariant. Then the phase of the block is rotated back by the estimated value.

A $Parameter$ block is a length-64 block containing controlling messages and train state information.

Two kinds of frames are involved in the proposed frame design: the data frame (DF) and the empty frame (EF). DFs containing user data can be transmitted bi-directionally between TUs and RUs. EFs are designed for the interaction of channel state information (CSI) and train state information (TSI) between TUs and RUs.

As depicted in Fig. 3, a $GI + Data$ block consists of a $Data$ block appended with a GI block. A CEF is inserted to every m $GI + Data$ blocks to form a $Data$-CEF combination. A data frame begins with a STF and a CEF, and then n $Data$-CEF combinations with GIs are attached successively. Number n is determined by the overall throughput of upper layer services, and the determination of m should be based on extensive channel measurements and simulations to achieve a good tradeoff between spectrum efficiency and system performance in fast varying channels.

D. Frame Synchronization and Channel Estimation

The detection of the arrival of a frame is accomplished by detecting the STF at the beginning of each frame taking advantage of the periodic feature of the STF [70]. Then, by applying (2) with the Ga_{128} and Gb_{128} blocks contained in the length-512 CEF Golay sequence, channel estimation is performed to attain a length-128 complex CIR. The time resolution of the attained CIR is highly dependent on the system bandwidth and sampling rate of the analog-digital converter (ADC). For example, for a system with 1 GHz bandwidth and ADC sampling rate 2 GHz, the time resolution of the CIR is 0.5 ns and the time span of each estimated CIR is 128 ns. As mentioned in previous measurement studies [11], [39], the excess delay of mmWave propagation in outdoor environments can be as high as hundreds of nanoseconds due to the arrival of clusters after long-distance transmission. However, we do not suggest increasing the CEF length to enable the detection of those clusters for the concern of system efficiency and the negligible impacts of those clusters.

E. Fractionally Spaced Equalization

Conventionally, equalization algorithms are based on symbol spaced sampling where the sampling frequency of the analog-to-digital converter (ADC) equals the symbol rate [73]. Those conventional equalizers are called symbol spaced equalizers (SSEs). However, SSEs are extremely sensitive to sampling time jitter, especially in mmWave systems where the symbol rate reaches Gbps level, and stringent timing recovery circuits are required to estimate the sampling deviation first, and then adjust the VCO oscillator frequency of ADC. This method will introduce large delay to the communication system. Hence, as an alternative approach, fractionally spaced equalization (FSE) where the input signal of ADC is sampled at twice the symbol rate is employed in our system to compensate for any timing phase or phase distortion before the received signal is sampled by the symbol rate. As FSE is already a matual technology and widely used in various scenarios, such as optical communications [74], bit-patterned media recording (BPMR) [75], and mobile underwater acoustic communications [76], details about the designing of FSE is not

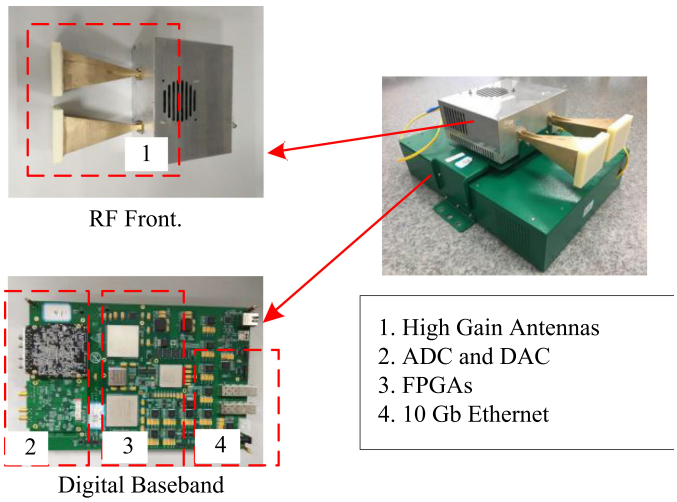

Fig. 4. Hardware prototype of the mmWave system for HST communications.

TABLE I
THE KEY PARAMETERS OF THE SYSTEM PROTOTYPE FOR MMWAVE HST COMMUNICATION

Parameter	Value	Unit
Millimeter-wave Frequency	40.5-41.5	GHz
RF Output Power @41GHz	14.3	dBm
RX Sensitivity	-90	dBm
Receiver Gain	53	dBm
Antenna Gain	24.50	dBi
HPBW	10	degree
Bandwidth	1.25	GHz
Intermediate Frequency (Transmitter)	0.5-1.5	GHz
Intermediate Frequency (Receiver)	2.5-3.5	GHz
Transmission Technology	Single Carrier (SC)	
Modulation Scheme	QPSK	
LDPC Rate	1/2	
Roll-off factor or RC filter	0.25	

discussed in this paper. Interested readers can refer to [74]–[76] for more information.

F. LDPC Decoding Using Stochastic Computation

In our system, the LDPC decoder is implemented using stochastic computing techniques. The core algorithm for the LDPC decoder is the well-known sum-product algorithm, which is a messaging-passing algorithm where probability messages about the correctness of the received symbols are exchanged iteratively between variable nodes and parity-checking nodes. In our LDPC decoder, the probabilities are represented by stochastic bit streams and stochastic computing techniques are utilized for probability calculation, resulting in simpler circuits and lower power consumption. Interested researchers can refer to [77]–[81] for more detailed information.

G. Hardware Prototype

The Hardware Prototype of the proposed mmWave wireless transceiver is shown in Fig. 4. The RF front-end is composed of several integrated chips, including the STUW81300 Microwave phase locked loop (PLL), the CHX2092a frequency multiplier, the HMC329 mixer, and a pair of TX-RX high gain (24.5 dBi) antennas whose azimuth and elevation half-power beamwidths (HPBWs) are 9.8° and 10.4° respectively, as depicted in Fig. 2. The digital baseband consists of an analog-to-digital converter (ADC) AD6688, a digital-to-analog converter (DAC) AD9163, two XC7VX690T FPGAs, and a ZYNQ-7045 chip. The key technologies, including the synchronization, channel estimation, equalization, and LDPC decoding blocks are implemented in those two XC7VX690T chips. An ARM Cortex-A9 dual-core processor integrated in the ZYNQ-7045 chip plays the role of central processing unit, which is responsible for system control and bridging the transceiver to upper layer applications. Both the RF front-end and the digital baseband are sealed in a cabinet to which a 10-Gigabits (10 Gb) optical interface is attached. Through the 10 Gb Ethernet the mmWave transceiver is able to communicate with upper layer services via optical fibers. The key parameters of the system are given in Table I.

IV. CHANNEL MEASUREMENTS AND ANALYSIS

As mentioned in Section II-A, existing mmWave measurement studies mainly focus on scenarios (such as the urban microcell scenario) where the relative speed between TX and RX is assumed to be $<$10 km/s. A lack of measurement research on mmWave channel characteristics in high-mobility scenarios becomes a stumbling block in the design of mmWave system for HST. Thus, this section provides the channel measurement results and analyses obtained when the TX-RX relative speed reaches 170 km/h. Our focus is placed on the power delay profile (PDP), root mean square delay spread (RMS-DS), fade depth (FD), small scale fading statistics, autocovariance function (AF), level crossing rate (LCR) and average fading duration (AFD) of the wireless channel.

A. Measurement Environment

The measurement campaign was conducted in a 2 km straight section in the Tianfu Avenue, Chengdu, China. As depicted in Fig. 5, the total width of the avenue is 86 m, with its two-way lines separated by a line separator that is covered with vegetation. The width of the line separator is 8.5 m. During the measurement, both the mmWave TX and RX antennas are fixed to the tops of two vehicles, whose heights are approximately 2 m above the ground. Those two vehicles are driven towards each other and the relative speed between them exceeds 170 km/h. A global-positioning-system (GPS) based distance measuring instrument is used to measure the distance between those two vehicles. To capture the small scale fading characteristics at a high relative speed between the transmitter and the receiver, the TX sends an empty frame per 38.816 μs and the RX estimates the channel impulse responses (CIRs) with a length-128 Golay correlator based on the CEF section in the empty frame. Hence, the time interval between two estimated CIRs is 38.816 μs, which is enough for the characterization of the fading channel. Thanks

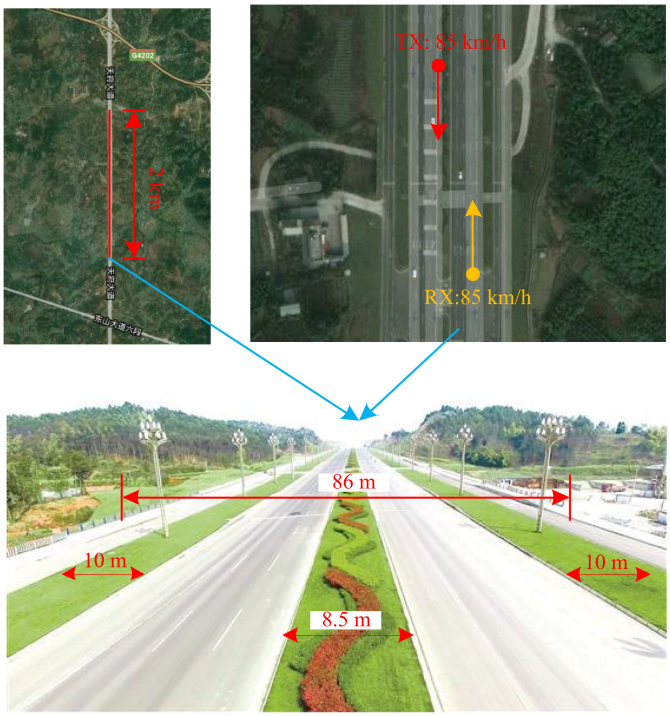

Fig. 5. Top left: satellite imagery of the 2 km straight section where the measurement campaign is conducted in Tianfu Avenue, Chengdu, China. Top right: the travelling speeds and directions of TX and RX. Bottom: A photograph of Tianfu Avenue.

to the high sampling rate of the ADC, the delay resolution of each CIR reaches 0.5 ns so that the CIR characteristics can be revealed detailedly.

As mentioned in Section II-B, the inter-RU distance of a HST system reaches 580 m. Moreover, some overlap between the coverage area of two successive RUs is required to reduce the difficulty in designing handover algorithms. Thus, we start recording the wireless channel when the TX-RX distance is above 1 km to investigate the long-distance propagation characteristics at the 41 GHz mmWave frequency. The antenna height difference between our measurement setup and a HST system could be assumed as negligible at such a long transmission distance. A total number of 20000 CIRs are recorded during the measurement.

B. Power Delay Profile

For a wideband transmission system, the complex low pass impulse response of a wireless channel can be modeled by

$$h\left(t,\tau\right)=\sum_{n=0}^{N}\alpha_n e^{j\phi_n(t)}\delta\left(\tau-\tau_n\right), \tag{3}$$

where N denotes the number of multipaths, and α_n, ϕ_n, τ_n denote the amplitude, phase and arrival time of the nth path respectively.

The information on the power of the arriving multipath is given in the power-delay profile (PDP), denoted as $P\left(\tau\right)=\left|h\left(t,\tau\right)\right|^2$.

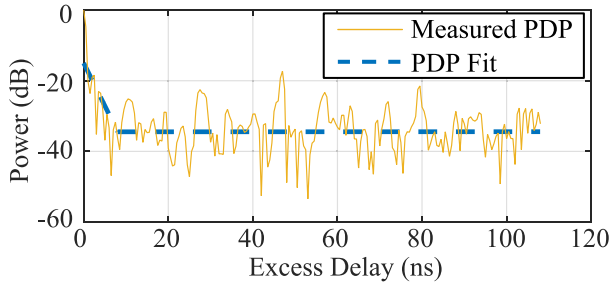

Fig. 6. Example of the measured PDP and the corresponding fitting with the 2-section exponential decay model in dB.

A very common approximation to the power delay profile is the exponential decay [82], [83]:

$$P\left(\tau\right)=\left|h\left(t,\tau\right)\right|^2\approx A\exp\left(-B\tau\right), \tag{4}$$

To characterize the PDP shapes more accurately, another model has been proposed and employed in [35], [84], i.e.,

$$P\left(\tau\right)=\begin{cases}0 & \tau<0\\ 1 & \tau=0\\ \Pi & 0<\tau<\tau_c\\ \Pi\exp\left(-B\left(\tau-\tau_c\right)\right) & \tau\geq\tau_c\end{cases}, \tag{5}$$

where Π is a constant independent of τ and $P\left(\tau\right)$ is normalized to the greatest multipath power $P\left(0\right)$ so that $P\left(0\right)=1$.

In this paper, we propose a more general PDP model for a better characterization of the PDP, and this model is called the 2-section exponential model, which is given as

$$P\left(\tau\right)=\begin{cases}0 & \tau<0\\ 1 & \tau=0\\ A_1\exp\left(-B_1\tau\right) & 0<\tau<\tau_c\\ P\left(\tau_c\right)\exp\left(-B_2\left(\tau-\tau_c\right)\right) & \tau\geq\tau_c\end{cases}, \tag{6}$$

where B_1, A_1, B_2, and τ_c are the PDP shape parameters whose distributions are to be analyzed. Clearly, the exponential decay in (4) can be viewed as the special case of (6) with $\tau_c=\infty$. The same is true to (5), which can be viewed as a 2-section exponential model with $B_1=0$.

Fig. 6 gives an example of the measured PDP and the corresponding model fitting according to (6). It can be seen that the measured PDP can be well fitted by the 2-section exponential decaying. Compared with this single example, the distributions of decaying parameters B_1, A_1, B_2, and τ_c and the relation among them are of greater importance. Fig. 7 depicts the measured cumulative distribution functions (CDFs) and the corresponding model fittings of the PDP shape parameters B_1, A_1, B_2, and τ_c. We can observe that B_1, A_1, and τ_c can be modeled by lognormal distributions $N_{log}\left(-0.42,0.16^2\right)$, $N_{log}\left(-2.77,0.50^2\right)$ and $N_{log}\left(1.96,0.12^2\right)$, respectively. Since B_2 has negative measured values, it is fitted with normal distribution $N\left(0.0042,0.0060^2\right)$ and the model matches well with the measured distribution. It is interesting to find that the value of B_2 is very close to zero, indicating the PDP reaches the noise floor at a excess delay above τ_c. The expectation of a lognormal

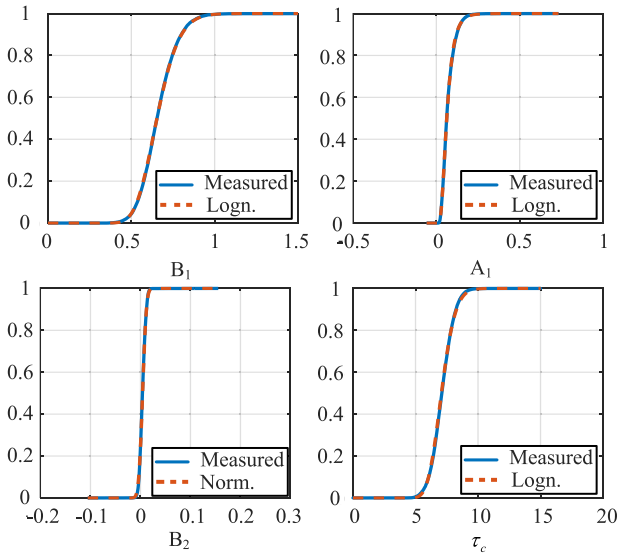

Fig. 7. Measured CDFs of PDP shape parameters B_1, A_1, B_2, and τ_c and the corresponding best-fitted lognormal/normal CDFs: $N_{log}(-0.42, 0.16^2)$, $N_{log}(-2.77, 0.50^2)$, $N(0.0042, 0.0060^2)$, and $N_{log}(1.96, 0.12^2)$, respectively.

distributed variable $X \sim N_{\log}\left(\mu, \sigma^2\right)$ can be calculated as

$$\mathbb{E}\left(X\right) = \exp\left(\mu + \frac{1}{2}\sigma^2\right), \tag{7}$$

based on which we can find the mean values of B_1, A_1 and τ_c are 0.66, 0.07 (-11.55 dB) and 7.13 ns, respectively. So the first arriving path at 0 ns is 11.55 dB stronger than the arriving path at 0.5 ns, and the PDP reaches the noise floor at 7.15 ns on average. It can also be calculated that the first arriving path is on average 33.37 dB above the noise level. Note that Golay correlator has a magnifying effect on the signal-to-noise power ratio (SNR). For each CIR, its SNR at the output of a Golay correlator will be magnified by a factor of $2N$, with N denoting the length of the complementary sequence. Thus, although the strongest path is 33.37 dB above the noise floor, the actual power difference between the strongest path and the noise floor is 9.29 dB.

The PDP shape parameters are essentially mutually correlated random variables. The cross correlation coefficient between two random variables X and Y is defined as

$$\rho\left(X, Y\right) = \frac{\sum_{n=1}^{N_S}\left(X_n - \overline{X}\right)\left(Y_n - \overline{Y}\right)}{\sqrt{\sum_{n=1}^{N_S}\left(X_n - \overline{X}\right)^2 \sum_{n=1}^{N_S}\left(Y_n - \overline{Y}\right)^2}}, \tag{8}$$

where X_n and Y_n denote the nth measured samples for X and Y, and $\overline{X}$ and $\overline{Y}$ denote the sample means of X and Y with the set size of N_S respectively.

The statistical characteristics including the mean, maximum, minimum, and standard deviation values, of the PDP shape parameters B_1, A_1, B_2, and τ_c, and their pair-wise cross correlation coefficients are listed in Table II. It can be seen that B_1 and A_1 are highly correlated with the cross correlation coefficient between them greater than 0.5, whereas B_2 is weakly correlated

TABLE II
STATISTICAL CHARACTERISTICS OF THE PDP SHAPE PARAMETERS

Statistical Characteristics				
Parameters	Mean	Max	Min	Standard Deviation
B_1	0.66	4.12	0.35	0.11
A_1	0.07	0.67	0.01	0.04
B_2	0.00	0.13	-0.08	0.01
τ_c	7.13	12.10	1.26	0.88
Cross Correlation Coefficients				
–	B_1	A_1	B_2	τ_c
B_1	1.00	0.75	0.05	-0.40
A_1	–	1.00	-0.01	-0.17
B_2	–	–	1.00	-0.52
τ_c (ns)	–	–	–	1.00

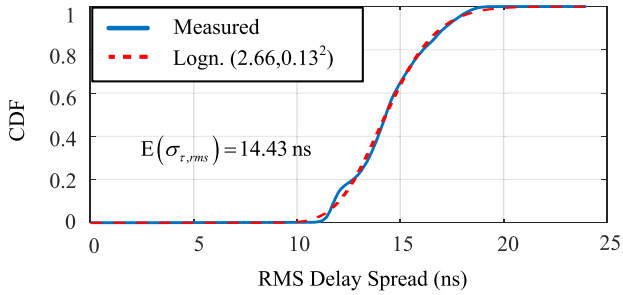

Fig. 8. A compare of the overall CDF of measured RMS delay and the CDF of lognormal distribution $N_{log}(2.66, 0.13^2)$.

with B_1 and A_1 with the cross correlation coefficients $\rho\left(B_2, B_1\right)$ and $\rho\left(B_2, A_1\right)$ smaller than 0.1. The little correlation between B_2 and B_1/A_1 is reasonable considering $B_2 \approx 0$ denotes the slope of the noise floor, and the noise is actually independent of the wireless channel.

C. RMS Delay Spread

Root-mean-square (RMS) delay spread characterizes the delay dispersion of the wireless channel. With the CIR $h\left(t, \tau\right)$ obtained, the RMS delay spread can be calculated by [85]

$$\tau_{rms} = \sqrt{\frac{\sum_k \left|h\left(t, \tau_k\right)\right|^2 \tau_k^2}{\sum_k \left|h\left(t, \tau_k\right)\right|^2} - \left(\frac{\sum_k \left|h\left(t, \tau_k\right)\right|^2 \tau_k}{\sum_k \left|h\left(t, \tau_k\right)\right|^2}\right)^2}, \tag{9}$$

where τ_k and $\left|h\left(t, \tau_k\right)\right|$ are the delay and amplitude of the kth path, respectively.

The CDF of the measured RMS delay spread is depicted in Fig. 8. It is shown that the RMS delay value ranges from 10 ns to 25 ns with mean 14.43 ns, and the measured CDF can be fitted with the lognormal distribution $N_{log}\left(2.66, 0.13^2\right)$. The measured RMS delay value gives insight to our system design in terms of determining the length of GI. As mentioned in Sec. III-C, the length of GI is 64, which corresponds to 64 ns with a transmission rate of 1 Gbps. Thus, it can be seen that the length of GI is much greater than the RMS delay sread, and is

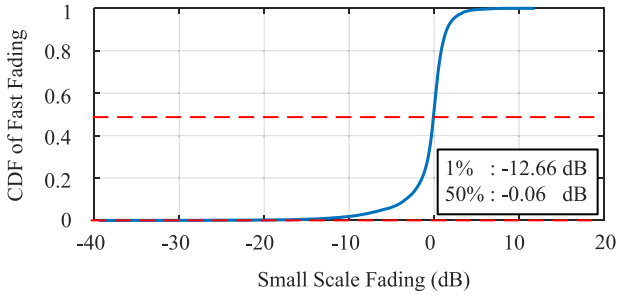

Fig. 9. Cumulative distribution function of small scale fading, obtained after taking the large scale values away from the received power with a window of 40 wavelengths.

enough for protecting the transmitted data against inter-symbol-interference.

D. Fade Depth

Fade depth (FD), which is defined as the difference in energy levels in dB between the 50% and 1% level values [29], [86], is an important parameter to measure the small-scale variation level in the channel energy. To obtain the FD for the wireless channel, the effect of large scale path loss and shadow fading should be removed at first, and the sliding window approach is often adopted [29]. In our case, we employ the sliding window approach with a window span of 40 wavelengths, which has proven to work well in previous measurement studies at conventional bands [29], [87] and some other frequencies such as 15 GHz [88].

Fig. 9 depicts the CDF of the channel energy level smoothed with the sliding window and normalised with respect to the average power in this window. The 50% and 1% levels are also marked out with red dashed lines. It can be seen that the 50% and 1% levels correspond to the power levels of -0.06 db and -12.66 dB, respectively, and we can find $FD = 12.6$ dB. FD reflects the intensity of vibration of the channel energy due to the multipath effect. From our analysis, we can see that the destructive interference of multipath can cause a fading as deep as 12.6 dB.

E. Best Fit Distribution of Small Scale Fading

To obtain the statistical characteristics of the small scale fading, we consider three widely used candidate distributions: the Rice, the Rayleigh, and the lognormal distribution [29], [89]. For each CIR, the channel transfer function can be obtained by taking the CIR into discrete-time Fourier transform (DTFT), i.e., $H(t,k) = \sum_{n=1}^{N} h(t,\tau_n) e^{-\frac{j2\pi kn}{N}}$. We only consider the distribution of $H(t,1)$ obtained from each CIR to avoid double counting of transfer functions that fall in the same coherence bandwidth. In the post processing, Akaike's information ceiteria (AIC) [29], [87], [89] is applied to select the model from the three candidate distributions that best fits the empirical distribution of the small scale fading. The AIC for the j-th candidate

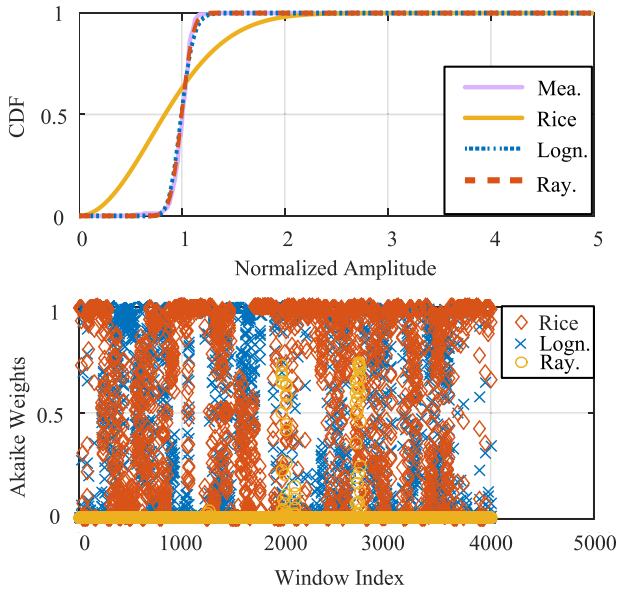

Fig. 10. Top: A example of the measured CDF (Mea.) in the 1000th sliding window and the corresponding best fitted Rice (Rice), Rayleigh (Ray.), and lognormal (Logn.) CDF models. Bottom: Akaike weights for three candidate distributions.

distribution is given by

$$\mathrm{AIC}_j = -2\sum_{n=1}^{N} \log_e\left(g_{\hat{\theta}_j}(x_n)\right) + 2U, \tag{10}$$

where $g_{\hat{\theta}_j}(x)$ denotes the probability density function (PDF) of x; $\hat{\theta}_j$ denotes the maximum likelihood (ML) estimation of the distribution parameter vector θ_j; N denotes the size of the sample set and U denotes the dimension of θ_j. The Akaike weight [29], [87] can better compare the relative fit of multiple distributions in the candidate set:

$$w_j = \frac{\exp\left(-(\mathrm{AIC}_j - \min_i \mathrm{AIC}_i)/2\right)}{\sum_{k=1}^{J} \exp\left(-(\mathrm{AIC}_k - \min_i \mathrm{AIC}_i)/2\right)}, \tag{11}$$

where we have $\sum_{j=1}^{J} w_j = 1$ and the model with the highest Akaike weight can be considered as the best-fitted distribution.

Fig. 10 (Top) gives an example of the empirical CDF and the best-fitted Rice, Rayleigh, and lognormal CDF models based on the measurements in the 1000-th sliding window, it can be seen that both the Rice and the lognormal model match well with the empirical CDF. However, from Fig. 10 (Bottom), which gives the Akaike weights for the three candidates obtained from 4000 sliding windows, it can be seen clearly that the Rice distribution can model the empirical distribution better than the lognormal distribution.

Table III lists the percentage of the best fit for the Rice, Rayleigh, and lognormal distributions. It can be seen that 62.8% of the small-scale fading can be best modelled with the Rice distribution. The predominance of the Rice distribution implies the existence of a steady arriving path. This is reasonable because the TX-RX antennas are pointed to each other during the recording of CIRs so that LoS propagation can be assumed. In fact, LoS

TABLE III
RATE OF SMALL-SCALE BEST FIT DISTRIBUTIONS

Distribution Type	Percentage
Rice	62.8%
Rayleigh	1.0%
Percentage	36.2%

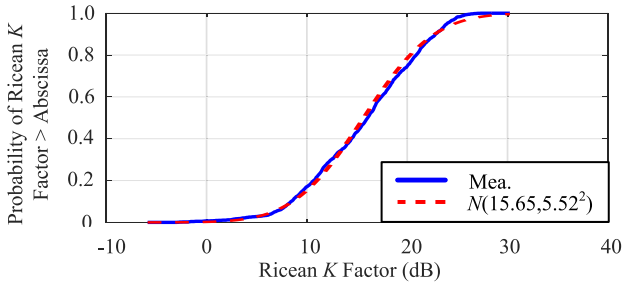

Fig. 11. CDF of Ricean K Factor, obtained from the measurements in windows where the Rice distribution shows the best fit.

can be maintained for most of the time in HST communication [46]. Taking advantage of this feature of HST, the complexity and cost of mmWave systems for HST might be significantly reduced through proper system design.

F. Ricean K Factor

For these cases in which the empirical CDF is best fitted by the Rice distribution, the Ricean *K* factor can be estimated by [90]

$$\hat{K}_{2,4} = \frac{-2\hat{\mu}_2^2 + \hat{\mu}_4 - \hat{\mu}_2\sqrt{2\hat{\mu}_2^2 - \hat{\mu}_4}}{\hat{\mu}_2^2 - \hat{\mu}_4} \tag{12}$$

where $\hat{\mu}_2$ and $\hat{\mu}_4$ are the estimation of the second order moment and the 4-th order moment respectively.

The CDF of the measured Ricean *K* factor obtained from windows where Rice distribution shows the best fit is depicted in Fig. 11. Our analysis shows that the empirical Ricean *K* factor ranges from -10 dB to 30 dB and can be well modeled with the Gaussian distribution with mean 15.65 dB and standard deviation 5.52 dB. Note that this distribution model for *K* is obtained when highly directive antennas are applied, whose beam pattern is depicted in Fig. 2, and when the TX-RX distance is above 1000 kilometers.

G. Coherence Time

Coherence time is an important parameter that describes the variation rate of the channel as a result of multipath propagation, the motion of the terminals and variations of the environments [36]. Coherence time can be calculated from the autocovariance function (ACF), which is defined as

$$\rho(\Delta t) = \frac{Cov\left[H(t), H(t+\Delta t)\right]}{\sqrt{Var\left[H(t)\right]}\sqrt{Var\left[H(t+\Delta t)\right]},} \tag{13}$$

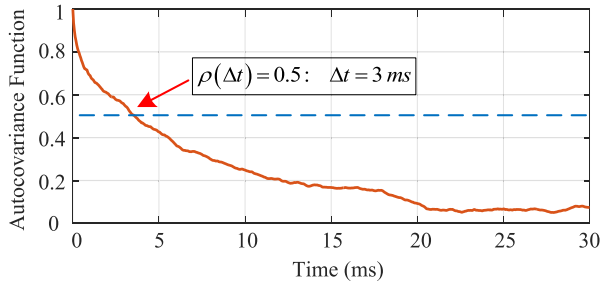

Fig. 12. Absolute value of the autocovariance function.

where $H(t)$ denotes the channel transfer function at time t, and $Cov[\cdot]$, $Var[\cdot]$ denote the covariance and variance functions, respectively.

With the ACF obtained, coherence time is defined as the value of Δt when $\rho(\Delta t) = 0.5$.

Fig. 12 depicts the absolute value of the empirical ACF, and also marks the level of $ACF = 0.5$. It can be seen that the measured coherence time is $\Delta t = 3$ ms. Note that coherence time can also be evaluated theoretically through [26]

$$\Delta t(\theta) = \frac{\sqrt{(4-\pi)/2\pi^2}}{f_D\sqrt{\left(1-\sin c^2\left(\frac{\theta}{2}\right)\right)\left(1-\frac{\sin c^2(\theta/2)-\sin c(\theta)}{1-\sin c^2(\theta/2)}\right)}}, \tag{14}$$

assuming that the gain within the beamwidth is uniform and is zero outside. It can be seen that the coherence time Δt is a function of both the beamwidth θ and the maximum Doppler frequency f_D. The maximum Doppler frequency can be evaluated with $f_D = \frac{f_c \times v}{c}$, where f_c, v, and c denote the carrier frequency, TX-RX relative velocity and the speed of light, respectively. Using the parameters listed in Table I, the theoretical coherence time of the proposed system is $\Delta t^{\text{th}} = 21$ ms, which is much greater than the measured value. The difference between the theoretical value and measured value of Δt might lie in the nonuniform distribution of antenna gain within the beamwidth.

H. Level Crossing Rate and Average Fading Duration

The level crossing rate (LCR) and average fading duration (AFD) show how often the received signal crosses a given energy threshold per time unit and for how long on average the signal is below a certain threshold [29]. In this paper, we give the LCR and AFD in terms of crossings per wavelength (C/W) and wavelengths per wavelength (W/W), respectively [29], [91], [92].

Fig. 13 gives the measured LCR in terms of C/W and the average fading duration in terms of W/W. It can be observed that at the threshold of 0 dB (the average receive energy), the empirical LCR grows to the highest level, which is slightly lower than 1 C/W. From the LCR vs. threshold curve we can also see the receive energy even crosses the threshold of -20 dB, but the LCR is small, indicating the crossings of the -20 dB level do not happen very often. The AFD vs. threshold curve shows that the time of the receive energy above 0 dB is longer than that below 0 dB. However, as 0 dB represents the average receive

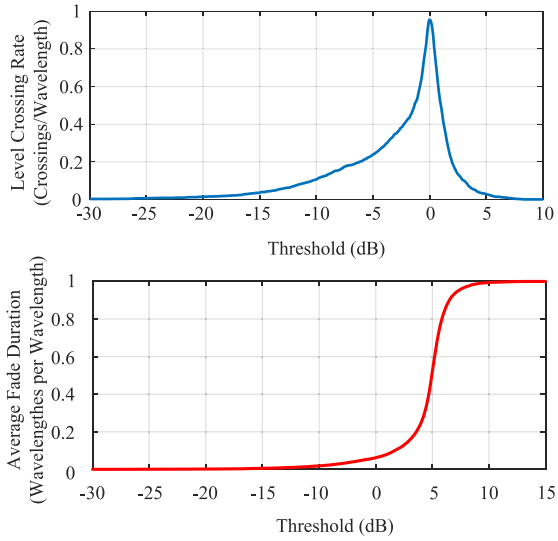

Fig. 13. Measured level crossing rate in terms of crossings per wavelength and average fade duration in terms of wavelengths per wavelength.

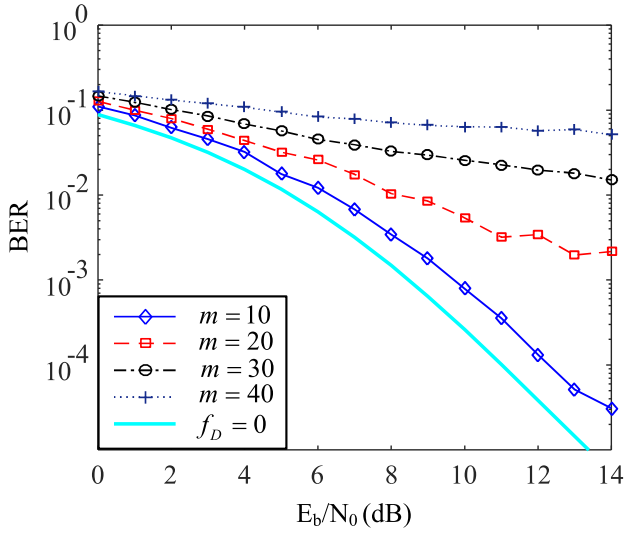

Fig. 14. Uncoded BER for the proposed mmWave HST communication scheme with m changing from 10 to 40 under Ricean fading channel with $K = 15$ dB.

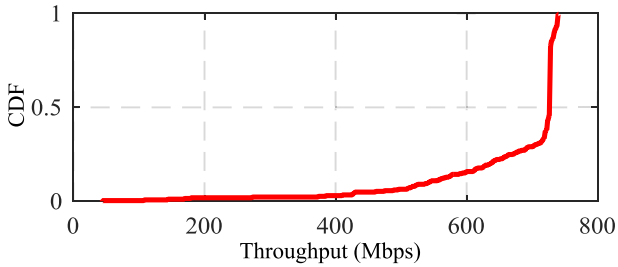

Fig. 15. CDF of system throughput recorded during the transmission of three HD video streams.

energy level, it could be expected that the destructive effects of the wireless channel is more severe than its constructive effects, but the former's frequency of occurrence is lower.

V. System Performance

A. BER Performance

The decision of some key parameters of the proposed system, such as m in Section III-C, is based on the simulation of the system's bit-error-rate (BER) performance. In the simulation, the Ricean channel with a Ricean K factor of 15 dB is applied. Considering the 1 Gbps bandwidth of our system and the PDP shape characteristics obtained from measurements (see Section IV-B), we adopt a total number of 5 multipaths and their power levels are allocated according to the measurement results presented in Section IV-B. Besides, the Doppler frequency is given as 100 kHz, which is much larger than the maximum Doppler frequency when the relative TX-RX speed reaches 500 km/h (which is 19 kHz).

As noted in Section III-C, a CEF is inserted to m (GI+$Data$) block to form a $Data$-CEF combination. The uncoded BER performance of the proposed system as m changes from 10 to 40 is given in Fig. 14. We also compare the BER performances for different m values with the ideal case when Doppler frequency $f_D = 0$, i.e., when the TX and RX can be viewed as relatively static to each other. It can be observed that as m decreases, the BER performance approaches that of the static case. Note that a decrease in m will result in a decrease of the system throughput. A detailed analysis of the system throughput measured when m is configured to 10 is provided in the following subsection.

B. System Throughput

Fig. 15 depicts the CDF of the system throughput[1] recorded during the transmission of three high-definition (HD) video streams using the system prototype established based on the proposed system design principles. Considering the system bandwidth of 1 GHz (QPSK modulation) and LDPC rate of $1/2$, the maximum achievable rate of the system is 1 Gbps. Besides, a physical layer frame consists of a length-2176 STF and ten length-5632 $Data$-CEF combinations. Each $Data$-CEF combination contains a length-512 CEF and ten length-512 GI+$Data$ blocks, where the length of a GI block is 64. Hence, the STF, CEF, and GI blocks in a data frame account for

$$\frac{2176_{(STF)}+10\times 512_{(CEF)}+100\times 64_{(GI)}}{2176_{(STF)}+10\times 5632_{(Data\_CEF)}}=23.4\% \quad (15)$$

of a data frame. So the maximum achievable upper layer user data rate is around 750 Mbps, which corresponds to the maximum throughput in Fig. 15.

C. Outage Probability

The outage probability (OP) of the mmWave system for HST is defined as the probability of the event when the received power falls to a level that is below the RX sensitivity. In this section, we give the OP as a function of TX-RX distance and PLE, where the free-space PL model [34], [93], [94]

$$\mathrm{PL}\left(f_c,d\right)=32.4+10n\log_{10}\left(d\right)+20\log_{10}\left(f_c\right) \quad (16)$$

[1]Here, the system throughout corresponds to the upper layer user data rate.

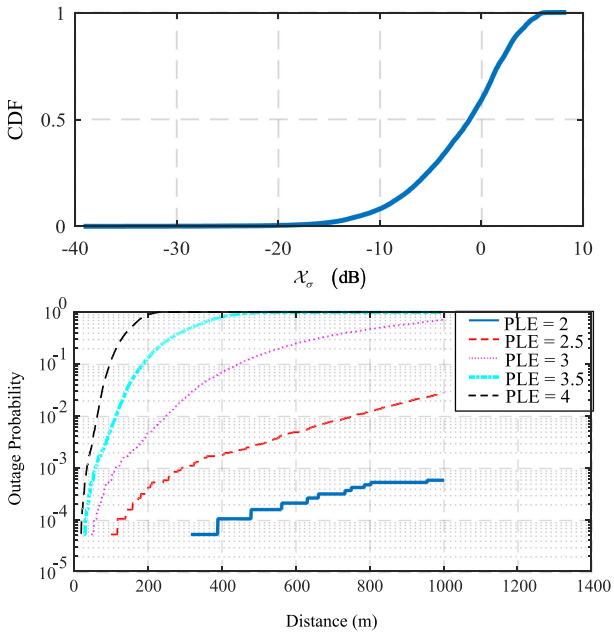

Fig. 16. Top: measured CDF of the addition of shadowing and small scale fading. Bottom: outage probability as a function of TX-RX distance and PLE.

is applied, and n, d and f_c denote the PLE, TX-RX distance (meters) and carrier frequency (GHz), respectively. With $\mathrm{PL}(f_c, d)$ available, OP can be estimated by

$$\mathrm{OP} = P_r\left\{\mathrm{PL}(f_c, d) + \mathcal{X}_\sigma > P_t + G_t + G_r - S\right\}, \quad (17)$$

where $P_r\{x\}$ denotes the probability that an event x happens; P_t, G_t, G_r and S denote the TX power (dBm), TX antenna gain (dBi), RX antenna gain (dBi) and RX sensitivity (dBm), respectively, whose values are listed in Table I. $\mathcal{X}_\sigma$ denotes the shadowing added with small scale fading in dB, which can be obtained by restoring the effect of shadow fading that is removed using a 40-wavelength sliding window in Section IV-D. As the inter-CIR time interval is merely 38.816 μs, and the relative TX-RX speed reaches 170 km/h when these CIRs are recorded, the inter-CIR space interval becomes 0.0018 meters. Thus, the 20000 recorded CIRs take a space span of merely 36 meters. Note that those 20000 CIRs are recorded when the TX-RX distance is above 1 km. Hence, the change of PL within the 20000 CIRs is limited to

$$10n\log_{10}\left(\frac{d+36}{d}\right) < 10n\log_{10}\left(\frac{1000+36}{1000}\right) = 0.1536n, \quad (18)$$

which is small and negligible. As a result, $\mathcal{X}_\sigma$ can be obtained by normalizing the measured channel energies of the 20000 CIRs with respect to their mean value.

Fig. 16 (top) depicts the CDF of $\mathcal{X}_\sigma$ obtained from the 20000 recorded CIRs. Fig. 16 (bottom) depicts the OP curves vs. d as n changes from 2 to 4. In open straight areas, such as the straight urban and rural scenarios for HST [18], the value of PLE is usually smaller than 2. So the OP can be limited to a low level ($<10^{-3}$) even at 1 km TX-RX distance. However, in some other environments such as curved tunnels, the value of PLE can be as large as 4 due to obstruction, multiple reflection and diffraction [18]. In these scenarios, The OP grows to a high level even when TX and RX are very close to each other ($<$200 meters). Thus, a dense distribution of RUs are required to safeguard the quality of service in these cases. Note that in HST applications, (16) is accurate when TX-RX distance is large enough ($>$200 meters), so that the impact of TX and RX antenna height difference could be ignored. However, when RX is close to TX, the TX-RX beam misalignment will result in a discrepancy between the practical path loss and the free space PL model, and might cause outage. In practical systems, this problem can be addressed by handover to the next RU.

VI. Conclusion

In this paper, a SC-FDE mmWave system operating at the 41 GHz band for HST radiocommunications between train and trackside is introduced. Some mature technologies such as FSE and stochastic computation based LDPC are employed to make a desirable tradeoff between system performance and complexity. Besides, a novel frame structure dedicated for mmWave HST communications is proposed. A system prototype established based on the proposed design principles is also presented.

This paper also gives the channel measurement results at the 41 GHz band obtained when the relative TX-RX velocity exceeds 170 km/h. The analysis of channel characteristics such as PDP, RMS-DS, FD, small scale fading statistics, AF, LCR, and AFD provides important guidelines for the design of mmWave systems for HST. Incorporating the channel measurement results, the system performances, including the BER performance, outage probability, and system throughput, are evaluated and analyzed.

In the near future, we will provide more system-level analysis e.g., packet delay and data loss tolerance. Besides, we will integrate higher order modulation schemes such as 16-QAM and 64-QAM into our system prototype to further boost the system throughput. In addition, we will conduct mmWave channel measurements in various HST scenarios.

Acknowledgment

We would like to thank Xiaohong Tang of University of Electronic Science and Technology of China for his help. This work might not have been possible had it not been for his efforts and support.

References

[1] K. Guan *et al.*, "On millimeter wave and THz mobile radio channel for smart rail mobility," *IEEE Trans. Veh. Technol.*, vol. 66, no. 7, pp. 5658–5674, Jul. 2017.
[2] J. Kim *et al.*, "A comprehensive study on mmWave-based mobile hotspot network system for high-speed train communications," *IEEE Trans. Veh. Technol.*, vol. 68, no. 3, pp. 2087–2101, Aug. 2018.
[3] A. Sniady and J. Soler, "An overview of GSM-R technology and its shortcomings," in *Proc. 12th ITS Telecommun.*, Nov. 2012, pp. 626–629.
[4] M. Chuang and M. Chen, "A mobile proxy architecture for video services over high-speed rail environments in LTE-A networks," *IEEE Syst. J.*, vol. 9, no. 4, pp. 1264–1272, Dec. 2015.
[5] M. Aguado *et al.*, "WiMax on rails," *IEEE Veh. Technol. Mag.*, vol. 3, no. 3, pp. 47–56, Sep. 2008.

[6] G. Barbu, "E-Train-broadband communication with moving trains," [Online]. Jun. 2010. Available: https://www.uic.org/

[7] K. Guan, Z. Zhong, and B. Ai, "Assessment of LTE-R using high speed railway channel model," in *Proc. 3rd Int. Conf. Commun. Mobile Comput.*, Qingdao, China, 2011, pp. 461–464.

[8] "HORIZON 2020 work programme 2014C2015 11. Smart, green and integrated transport revised," European Commission Decision, Tech. Rep. C(2014)4995, Jul. 2014.

[9] F. Hasegawa *et al.*, "High-speed train communications standardization in 3GPP 5G NR," *IEEE Commun. Standards Mag.*, vol. 2, no. 1, pp. 44–52, Mar. 2018.

[10] S. Choi, H. Chung, J. Kim, J. Ahn, and I. Kim, "Mobile hotspot network system for high-speed railway communications using millimeter waves," *ETRI J.*, vol. 38, no. 6, pp. 1052–1063, Dec. 2016.

[11] J. Ko *et al.*, "Millimeter-wave channel measurements and analysis for statistical spatial channel model in in-building and urban environments at 28 GHz," *IEEE Trans. Wireless Commun.*, vol. 16, no. 9, pp. 5853–5868, Jun. 2017.

[12] H. Tsuji, K. Tsukamoto, K. Suzuki, and H. Nagayama, "Development of high-speed mobile radio communication systems using 40 GHz frequency band," *Radio Sci.*, vol. 51, no. 7, pp. 1220–1233, Jul. 2016.

[13] K. Tsukamoto, "Field-test results of mobile communication systems over 40 GHz frequency band," *IEEE VTS APWC*, Aug. 2014, pp. 1–5.

[14] T. S. Rappaport, J. N. Murdock, and F. Gutierrez, "State-of-the-art in 60-GHz integrated circuits and systems for wireless communications," *Proc. IEEE*, vol. 99, no. 8, pp. 1390–1436, Aug. 2011.

[15] C. Dehos *et al.*, "Millimeter-wave access and backhauling: The solution to the exponential data traffic increase in 5G mobile communications systems," *IEEE Commnun. Mag.*, vol. 52, no. 9, pp. 88–95, Sep. 2014.

[16] Z. Y. Pi, J. Choi, and R. W. Heath, "Millimeter-wave gigabit broadband evolution toward 5G: Fixed access and backhaul," *IEEE Commnun. Mag.*, vol. 54, no. 4, pp. 138–144, Apr. 2016.

[17] The National Institute of Information and Communication Technology (NICT) in Japan, Proposal of a New Working Document of a Draft New APT Report on Millimeter-wave Band Railway Radiocommunication Systems Between Train and Trackside, and its Work Plan, *AWG-20*, 29 Aug. 2016.

[18] D. He *et al.*, "Channel measurement, simulation, and analysis for high-speed railway communications in 5G millimeter-wave band," *IEEE Trans. Intell. Transp. Syst.* vol. 19, no. 10, pp. 3144–3158, Oct. 2018.

[19] J. Yang *et al.*, "A geometry-based stochastic channel model for the millimeter-wave band in a 3GPP high-speed train scenario," *IEEE Trans. Veh. Technol.*, vol. 67, no. 5, pp. 3853–3865, Jan. 2018.

[20] K. Guan and G. Li, "Mobile channel characterization in typical subway tunnels at 30 GHz," *IEEE Tech. Rep. IEEE 802.15-15-0666-02-hrrc*, Sep. 2015, pp. 1–5.

[21] G. Li *et al.*, "Channel characterization for mobile hotspot network in subway tunnels at 30 GHz band," *IEEE Veh. Techn. Conf.*, Nanjing, China, May 2016, pp. 1–5.

[22] X. Lin *et al.*, "Measurement based ray tracer calibration and channel analysis for high-speed railway viaduct scenario at 93.2 GHz," in *Proc. IEEE Int. Symp. Ant. Propag. USNC/URSI Nat. Radio Sci. Meeting*, San Diego, USA, 2017, pp. 1947–1491.

[23] J. Kim and I. G. Kim, "Distributed antenna system-based millimeter-wave mobile broadband communication system for high speed trains," in *Proc. Int. Conf. ICT Converg. (ICTC)*, Jeju, South Korea, Oct. 2013, pp. 218–222.

[24] P. T. Dat, A. Kanno, N. Yamamoto, and T. Kawanishi, "WDM RoF-MMW and linearly located distributed antenna system for future high speed railway communications," *IEEE Commun. Mag.*, vol. 53, no. 10, p. 86C94, Oct. 2015.

[25] Y. Cui, X. Fang, and L. Yan, "Hybrid spatial modulation beamforming for mmWave railway communication systems," *IEEE Trans. Veh. Technol.*, vol. 65, no. 12, pp. 9597–9606, Dec. 2016.

[26] V. Va, X. Zhang, and R. W. Heath, Jr., "Beam switching for millimeter wave communication to support high speed trains," in *IEEE Proc. Veh. Technol. Conf.*, Boston, USA, Sep. 2015, pp. 1–5.

[27] C. Jiao, Z. Zhang, H. Zhang, L. Zhu, and C. Zhong, "A sequential antenna hopping scheme for high mobility MIMO communications," in *Proc. IEEE Int. Conf. Commun.*, London, U.K., Jun. 2015, pp. 4984–4989.

[28] C. Wang *et al.*, "Channel measurements and models for high-speed train communication systems: A survey," *IEEE Commun. Surveys Tut.*, vol. 18, no. 2, pp. 974–987, Dec. 2015.

[29] R. He *et al.*, "Measurements and analysis of propagation channels in high-speed railway viaducts," *IEEE Trans. Wireless Commun.*, vol. 12, no. 2, pp. 794–805, Dec. 2012.

[30] A. Ghazal *et al.*, "A non-stationary MIMO channel model for high-speed train communication systems," in *Proc. 75th IEEE VTC Spring*, Yokohama, Japan, 2012, p. 1C5.

[31] L. Liu *et al.*, "Position-based modeling for wireless channel on high-speed railway under a viaduct at 2.35 GHz," *IEEE J. Sel. Area Commun.*, vol. 30, no. 4, pp. 834–845, Apr. 2012.

[32] B. Ai *et al.*, "Measurement and analysis of extra propagation loss of tunnel curve," *IEEE Trans. Veh. Technol.*, vol. 65, no. 4, pp. 1847–1858, Apr. 2016.

[33] T. S. Rappaport *et al.*, "Wideband millimeter-wave propagation measurements and channel models for future wireless communication system design," *IEEE Trans. Commun.*, vol. 63, no. 9, pp. 3029–3056, Sep. 2015.

[34] G. Maccartney, T. S. Rappaport, and A. Ghosh, "Base station diversity propagation measurements at 73 GHz millimeter-wave for 5G coordinated multipoint (CoMP) analysis," in *Proc. GLOBECOM Workshops IEEE*, Singapore, Dec. 2017, pp. 1–7.

[35] H. Yang, P. F. M. Smulders, and M. H. A. J. Herben, "Channel characteristics and transmission performance for various channel configurations at 60 GHz," *EURASIP J. Wirel. Commun. Netw.*, vol. 2007, no. 1, pp. 43–58, Jan. 2017.

[36] T. S. Rappaport, R. W. Heath, Jr., R. C. Daniels, and J. N. Murdock, *Millimeter Wave Wireless Communications.* Englewood Cliffs, NJ, USA: Prentice Hall, 2015.

[37] P. F. M. Smulders and L. M. Correia, "Characterisation of propagation in 60 GHz radio channels," *Electron. Commun. Eng. J.*, vol. 9, no. 2, pp. 73–80, Apr. 1997.

[38] H. J. Liebe, "Molecular transfer characteristics of air between 40 and 140 GHz," *IEEE Trans. Microw. Theory Techn.*, vol. 23, no. 4, pp. 380–386, Apr. 1975.

[39] T. S. Rappaport *et al.*, "Overview of mmWave communications for fifth-generation (5G) wireless networks with a focus on propagation models," *IEEE Trans. Antennas Propag.*, vol. 65, no. 12, pp. 6213–6230, Dec. 2017.

[40] Q. Zhao and J. Li, "Rain attenuation in millimeter wave ranges," in *Proc. Int. Symp. Antennas Propag. EM Theory*, Oct. 26–29, 2006, pp. 1–4.

[41] M. Kyro *et al.*, "Long range wideband channel measurements at 81–86 GHz frequency range," in *Proc. 4th EuCAP*, Apr. 2010, p. 1C5.

[42] J. S. Lu, D. Steinbach, P. Cabrol, and P. Pietraski, "Modeling human blockers in millimeter wave radio links," *ZTE Commun.*, vol. 10, no. 4, pp. 23–28, 2012.

[43] H. Zhao *et al.*, "28 GHz millimeter wave cellular communication measurements for reflection and penetration loss in and around buildings in New York city," in *Proc. IEEE ICC*, Budapest, Hungary, Jun. 2013, pp. 5163–5167.

[44] F. Wang and K. Sarabandi, "An enhanced millimeter-wave foliage propagation model," *IEEE Trans. Antennas Propag.*, vol. 53, no. 7, pp. 2138–2145, Jul. 2005.

[45] B. Ai *et al.*, "Radio wave propagation scene partitioning for high-speed rails," *Int. J. Antennas Propag.*, vol. 2012, no. 815232, pp. 7–22, May 2012.

[46] B. Chen *et al.*, "Channel characteristics in high-speed railway: A survey of channel propagation properties," *IEEE Veh. Tech. Mag.*, vol. 10, no. 2, pp. 67–68, May 2015.

[47] B. Ai *et al.*, "Challenges toward wireless communications for high-speed railway," *IEEE Trans. Intell. Transp. Syst.*, vol. 15, no. 5, pp. 2143–2158, Oct. 2014.

[48] J. Zhao *et al.*, "A dual-link soft handover scheme for C/U plane split network in high-speed railway," *IEEE Access*, vol. 6, pp. 12473–12482, Mar. 2018.

[49] H. Nishimoto *et al.*, "Linear cellularization enabling millimeter-wave train radio communication systems in 5G era," in *Proc. Progress Electromagn. Res. Symp.*, Toyama, Japan, Aug. 2018, pp. 99–106.

[50] F. Hasegawa *et al.*, "3GPP standardization activities in relay based 5G high speed train scenarios for the SHF band," *IEEE CSCN*, Helsinki, Finland, Aug. 2017, pp. 126–131.

[51] 3GPP, "Study on scenarios and requirements for next generation access technologies," 3GPP, Tech. Rep. 3GPP TR 38.913 (V14.3.0), Aug. 2017.

[52] P. T. Dat *et al.*, "High-capacity wireless backhaul network using seamless convergence of radio-over-fiber and 90-GHz millimeter-wave," *J. Lightw. Technol.*, vol. 32, no. 20, Oct. 2014, Art. no. 0733C8724.

[53] T. L. Thanh *et al.*, "10-Gb/s wireless signal transmission over a seamless IM/DD Fiber-MMW system at 92.5 GHz," in *Proc. IEEE ICC*, London, U.K., Jun. 2015, pp. 1364–1369.
[54] J. Kim, H. S. Chung, S. W. Choi, I. G. Kim, and Y. Han, "Mobile hotspot network enhancement system for high-speed railway communication," in *Proc. 11th Eur. Conf. Antennas Propag. (EuCAP)*, Paris, France, Mar. 19–24, 2017, pp. 2885–2889.
[55] S. Kutty and D. Sen, "Beamforming for millimeter wave communications: An inclusive survey," *IEEE Commun. Surveys Tut.*, vol. 18, no. 2, pp. 949–973, Dec. 2015.
[56] H. Yang, M. H. A. J. Herben, I. J. A. G. Akkermans, and P. F. M. Smulders, "Impact analysis of directional antennas and multiantenna beamformers on radio transmission," *IEEE Trans. Veh. Technol.*, vol. 57, no. 3, pp. 1695–1707, May 2008.
[57] S. Han, I. Chih-Lin, Z. Xu, and C. Rowell, "Large-scale antenna systems with hybrid analog and digital beamforming for millimeter wave 5G," *IEEE Commun. Mag.*, vol. 53, no. 1, pp. 186–194, Jan. 2015.
[58] R. Mndez-Rial *et al.*, "Hybrid MIMO architectures for millimeter wave communications: Phase shifters or switches?," *IEEE Access*, vol. 4, pp. 247–267, Jan. 2016.
[59] L. C. Godara, *Smart Antennas.* Boca Raton, FL, USA: CRC Press, 2004.
[60] J. Kim, H.-S. Chung, I. G. Kim, H. Lee, and M. S. Lee, "A study on millimeter-wave beamforming for high-speed train communication," in *Proc. Int. Conf. Inf. Commun. Technol. Convergence*, Jeju, South Korea, Oct. 2015, pp. 1190–1193.
[61] H. Song, X. Fang, and L. Yan, "Handover scheme for 5G C/U plane split heterogeneous network in high-speed railway," *IEEE Trans. Veh. Technol.*, vol. 63, no. 9, pp. 4633–4646, Nov. 2014.
[62] M. Polese *et al.*, "Improved handover through dual connectivity in 5G mmWave mobile networks," *IEEE J. Sel. Areas Commun.*, vol. 35, no. 9, pp. 2069–2084, Jun. 2017.
[63] A. Ghosh *et al.*, "Millimeter-wave enhanced local area systems: A high data-rate approach for future wireless networks," *IEEE J. Sel. Areas Commun.*, vol. 32, no. 6, pp. 1152–1163, Jun. 2014.
[64] Y. Lu *et al.*, "Remote antenna unit selection assisted seamless handover for high-speed railway communications with distributed antennas," in *Proc. IEEE 83rd Veh. Technol. Conf. (VTC Spring)*, Nanjing, China, May 2016.
[65] C. Z. Yang, L. H. Lu, C. Di, and X. M. Fang, "An on-vehicle dual-antenna handover scheme for high-speed railway distributed antenna system," in *Proc. Int. Wireless Commun. Mobile Comput. Conf. (IWCMC)*, Chengdu, China, Sep. 2010, pp. 1–5.
[66] X. Y. Qian, H. Wu, and J. Meng, "A dual-antenna and mobile relay station based handover in distributed antenna system for high-speed railway," in *Proc. Int. Conf. Innov. Mobile Internet Serv. Ubiq. Comput.*, Taiwan, China, Jul. 2013, pp. 585–590.
[67] J. Kim *et al.*, "A shared RUs based distributed antenna system for high-speed trains," in *Proc. IEEE Int. Symp. Consumer Electron.*, JeJu Island, South Korea, Jun. 2014, pp. 1–2.
[68] *Wireless LAN Medium Access Control (MAC) and Physical Layer (PHY) Specifications Amendment 3: Enhancements for Very High Throughput in the 60 GHz Band*, IEEE Standard 802.11ad-2012, 2012.
[69] N. Preyss and A. Burg, "Digital synchronization for symbol-spaced IEEE802.11ad Gigabit mmWave systems," in *Proc. IEEE Int. Conf. Electron. Circuits Syst. (ICECS)*, Cairo, Egypt, Dec. 2015, pp. 637–640.
[70] Y. S. Huang, W. C. Liu, and S. J. Jou, "Design and implementation of synchronization detection for IEEE 802.15.3c," in *Proc. Int. Symp. VLSI Design, Autom. Test (VLSI-DAT)*, Taiwan, China, Apr. 2011, pp. 1–4.
[71] C. F. Wu *et al.*, "Golay-correlator window-based noise cancellation equalization technique for 60 GHz wireless OFDM/SC receiver," *IEEE Trans. Very Large Scale Integr. Syst.*, vol. 24, no. 11, pp. 3323–3333, Nov. 2016.
[72] B. M. Popovic, "Efficient Golay correlator," *IEEE Electron. Lett.*, vol. 35, no. 17, pp. 1427–1428, Aug. 1999.
[73] J.-H. Park *et al.*, "A 2-Gb/s 5.6-mW digital equalizer for a LOS/NLOS receiver in the 60GHz band," in *Proc. IEEE Asian Solid-State Circuits Conf.*, Beijing, China, Nov. 2010, pp. 1–4.
[74] O. Zia-Chahabi *et al.*, "Efficient frequency-domain implementation of block-LMS/CMA fractionally spaced equalization for coherent optical communications," *IEEE Photon. Technol. Lett.*, vol. 23, no. 22, pp. 1697–1699, Nov. 2011.
[75] S. Koonkarnkhai *et al.*, "Study of fractionally spaced equalizers for bit-patterned media recording," *IEEE Trans. Mag.*, vol. 51, no. 11, Jun. 2015, Art. no. 3001604.
[76] J. Xi *et al.*, "Bidirectional fractionally-spaced decision feedback equalizer based on soft outputs combination," *Summit Int. Conf. Signal Inf. (ChinaSIP)*, Chengdu, China, Jul. 2015, pp. 948–952.
[77] R. Gallager, "Low-density parity-check codes," *IRE Trans. Inf. Theory*, vol. 8, no. 1, pp. 21–28, Jan. 1962.
[78] D. J. C. MacKay and R. M. Neal, "Near Shannon limit performance of low density parity check codes," *Electron. Lett.*, vol. 32, no. 18, pp. 1645–1646, 1996.
[79] S. S. Tehrani, S. Mannor, and W. J. Gross, "Fully parallel stochastic LDPC decoders," *IEEE Trans. Signal Process.*, vol. 56, no. 11, pp. 5692–5703, Nov. 2008.
[80] V. Gaudet and A. Rapley, "Iterative decoding using stochastic computation," *Electron. Lett.*, vol. 39, no. 3, pp. 299–301, Feb. 2003.
[81] S. S. Tehrani, A. Naderi, G.-A. Kamendje, S. Mannor, and W. J. Gross, "Tracking forecast memories in stochastic decoders," in *Proc. IEEE Int. Conf. Acoust. Speech Signal Process. (ICASSP)*, Taipei, Taiwan, Apr. 2009, pp. 561–564.
[82] A. M. Khattar, K. T. Wong, and Z. B. Li, "An integrated overview of the open literature's empirical data on the indoor radiowave channel's delay properties," *IEEE Trans. Antennas Propag.*, vol. 56, no. 5, pp. 1451–1468, May 2008.
[83] A. A. M. Saleh and R. A. Valenzuela, "A statistical model for indoor multipath propagation," *IEEE J. Sel. Areas Commun.*, vol. SAC-5, no. 2, pp. 128–137, Feb. 1987.
[84] K. Witrisal, G. Landman, and A. Bohdanowicz, "Practical application of a novel method for estimating the RMS delay spread from power measurements," in *Proc. EPMCC*, Vienna, Austria, Feb. 2001, pp. 1–5.
[85] A. F. Molisch, *Wireless Communications.* Hoboken, NJ, USA: Wiley, 2007.
[86] S. Kozono, "Received signal-level characteristics in a wide-band mobile radio channel," *IEEE Trans. Veh. Technol.*, vol. 43, no. 3, pp. 480–486, Aug. 1994.
[87] S. Lin *et al.*, "Finite-state Markov modeling for high-speed railway fading channels," *IEEE Antennas Wireless Propag. Lett.*, vol. 14, pp. 954–957, Apr. 2015.
[88] Q. Wang *et al.*, "Ray-based analysis of small-scale fading for indoor corridor scenarios at 15 GHz," in *Proc. IEEE Asia-Pacific Symp. Electromagn. Compat. (APEMC)*, Taipei, Taiwan, May 2015, pp. 181–184.
[89] S. Wyne, A. P. Singh, F. Tufvesson, and A. F. Molisch, "A statistical model for indoor office wireless sensor channels," *IEEE Trans. Wireless Commun.*, vol. 8, no. 8, pp. 4154–4164, Aug. 2009.
[90] C. Tepedelenlioglu and G. B. Giannakis, "The Ricean K factor: Estimation and performance analysis," *IEEE Trans. Wirless Commun.*, vol. 2, pp. 799–810, Jul. 2003.
[91] F. Perez-Fontan and P. M. Espineira, *Modelling the Wireless Propagation Channel: A Simulation Approach With MATLAB*. West Sussex, UK: Wiley, 2008, pp. 105–135.
[92] A. Abdi, K. Wills, H. A. Barger, M. S. Alouini, and M. Kaveh, "Comparison of the level crossing rate and average fade duration of Rayleigh, Rice, and Nakagami fading models with mobile channel data," in *Proc. IEEE VTC*, Sep. 2000, pp. 1850–1857.
[93] A. F. Molisch, A. Karttunen, S. Hur, J. Park, and J. Zhang, "Spatially consistent path loss modeling for millimeter-wave channels in urban environments," in *Proc. Eur. Conf. Antennas Propag. (EuCAP)*, Apr. 2016, vol. 16, no. 11, pp. 7538–7550.
[94] S. Sun *et al.*, "Investigation of prediction accuracy, sensitivity, and parameter stability of large-scale propagation path loss models for 5G wireless communications," *IEEE Trans. Veh. Technol.*, vol. 65, no. 5, pp. 2843–2860, May 2016.

Guangrong Yue received the Ph.D. degrees in communication and information system from the University of Electronic Science and Technology of China, Chengdu, China, in 2006.

He was a Postdoctoral Fellow with the Department of Electrical Engineering and Computer Science at the University of California Berkeley, from 2007 to 2008. He has been a Faculty Member in Telecommunications Engineering at the University of Electronic Science and Technology of China since 2008. His major research interests include wireless communication theory, millimeter wave communications, and adaptive signal processing.

Daizhong Yu received the B.S. degree from the University of Electronic Science and Technology of China, Chengdu, China, in 2016, and started the master program in 2016 in the National Key Laboratory of Communication, University of Electronic Science and Technology of China.

His current research interests include measurement and modeling of wireless propagation channels, high-speed railway communications, and millimeter-wave communication systems.

Long Cheng was born in Kaifeng. He received the B.E. degree in communication and information system from the University of Electronic Science and Technology of China, Chengdu, China, in 2016. He is currently working toward the Ph.D. degree with the University of Electronic Science and Technology of China.

His current research interests include millimeter-wave communications and high-speed railway communications.

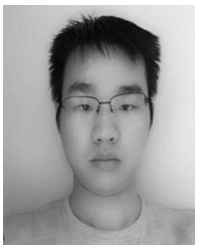

Qifu Lv received the bachelor's and master's degrees from Fuzhou University, Fuzhou, China and the University of Electronic Science and Technology of China, Chengdu, China in 2011 and 2014, respectively.

He joined Chengdu Glory Wireless Co. Ltd., Chengdu, China, in 2016, after three years with Zhuhai Allwinner Technology Co. Ltd., Zhuhai, China. His research interests include millimeter-wave communication, and digital circuit design.

Zhigang Luo received the bachelor's degree from the Wuhan University of Technology, Wuhan, China, in 2011 and master's degree from the Electronic Science and Technology University of China, Chengdu, China, in 2014.

He joined Glory Wireless Co. Ltd., Chengdu, China, in 2017, after three years with No. 30 Institute of CETC, Chengdu, China.

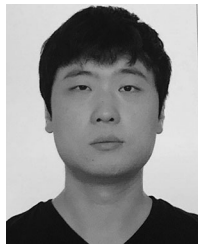

Qing Li received the bachelor's and master's degrees from the Electronic Science and Technology University of China, Chengdu, China, in 2010 and 2013, respectively.

He joined Chengdu Glory Wireless Co. Ltd., Chengdu, China, in 2017, after three years with Motorola Solutions Co. Ltd. and two years in Arraycom Co. Ltd. His research interests include millimeter-wave communication and parallel programming.

Junxin Luo received the bachelor's degree from Sichuan Normal University in 2005 and the master's degree from the Electronic Science and Technology University of China, Chengdu, China, in 2011.

He joined Shenzhen Y&D Electronics Information Co. Ltd., Shenzhen, China, in 2015, after three years with Chengdu Guoxing Communication Co. Ltd. and two years with Chengdu Anzhijie Technology Co. Ltd., Chengdu, China.

Xu He was born in Jintan, Jiangsu Province, China, on May 8, 1969. He received the master's degree from the University of Electronic Science and Technology, Chengdu, China, in 1994.

He is currently a Professor with the National Key Laboratory of Science and Technology on Communications, University of Electronic Science and Technology of China, Chengdu, China. His research interests include signal transmission by wireless channel, adapted digital signal processing technology, and hardware design technology, mainly on field program gate array design and printed circuit board design.